

INVESTIGATING GALACTIC SUPERNOVA REMNANT CANDIDATES USING LOFAR

LAURA N. DRIESSEN,^{1,2} VLADIMÍR DOMČEK,^{1,3} JACCO VINK,^{1,3,4} JASON W. T. HESSELS,^{1,5} MARIA ARIAS,¹ AND
JOSEPH D. GELFAND^{6,7}

¹*Anton Pannekoek Institute for Astronomy, University of Amsterdam, Science Park 904, 1098 XH Amsterdam, The Netherlands*

²*Jodrell Bank Centre for Astrophysics, School of Physics and Astronomy, The University of Manchester, Manchester, M13 9PL, UK*

³*GRAPPA, GRavitation and AstroParticle Physics Amsterdam, University of Amsterdam, Science Park 904, 1098 XH Amsterdam, Netherlands*

⁴*SRON, Netherlands Institute for Space Research, Sorbonnelaan 2, 3584 CA, Utrecht, The Netherlands*

⁵*ASTRON, Netherlands Institute for Radio Astronomy, Postbus 2, 7990 AA, Dwingeloo, The Netherlands*

⁶*NYU Abu Dhabi, PO Box 129188, Abu Dhabi, UAE*

⁷*Affiliate Member, Center for Cosmology and Particle Physics, New York University, 726 Broadway, New York, NY 10003*

(Received June 29, 2017; Accepted May 08, 2018)

Submitted to ApJ

ABSTRACT

We investigate six supernova remnant (SNR) candidates – G51.21+0.11, G52.37–0.70, G53.07+0.49, G53.41+0.03, G53.84–0.75, and the possible shell around G54.1+0.3 – in the Galactic Plane using newly acquired LOw-Frequency ARray (LOFAR) High-Band Antenna (HBA) observations, as well as archival Westerbork Synthesis Radio Telescope (WSRT) and Very Large Array Galactic Plane Survey (VGPS) mosaics. We find that G52.37–0.70, G53.84–0.75, and the possible shell around pulsar wind nebula G54.1+0.3 are unlikely to be SNRs, while G53.07+0.49 remains a candidate SNR. G51.21+0.11 has a spectral index of $\alpha = -0.7 \pm 0.21$, but lacks X-ray observations and as such requires further investigation to confirm its nature. We confirm one candidate, G53.41+0.03, as a new SNR because it has a shell-like morphology, a radio spectral index of $\alpha = -0.6 \pm 0.2$ and it has the X-ray spectral characteristics of a 1000–8000 year old SNR. The X-ray analysis was performed using archival *XMM-Newton* observations, which show that G53.41+0.03 has strong emission lines and is best characterized by a non-equilibrium ionization model, consistent with an SNR interpretation. Deep Arecibo radio telescope searches for a pulsar associated with G53.41+0.03 resulted in no detection, but place stringent upper limits on the flux density of such a source if it is beamed towards Earth.

Keywords: HII regions — ISM: supernova remnants — radio continuum: ISM — X-rays: ISM

arXiv:1706.08826v2 [astro-ph.HE] 9 May 2018

1. INTRODUCTION

There are many shell- and bubble-like objects in our Galaxy. For example, there are 295 supernova remnants (SNRs) in Green’s SNR catalog (just under half of which have only been detected in the radio; Green 2014, 2017), 76 SNR candidates in a recent THOR+VGPS analysis (Anderson, et al. 2017), and ~ 1500 known HII regions (as well as ~ 2500 probable and ~ 4000 candidate HII regions) in the WISE HII region catalog¹ (Anderson et al. 2014). This means that observations and surveys of the Galactic Plane capable of investigating shell-like objects, particularly observations differentiating between candidate HII regions and SNRs, are extremely useful. As there are many sources and candidates, targeting individual objects with a single pointing per object is impractical. Interferometers that can observe large areas of the sky at low-frequencies with wide frequency bandwidth should prove to be excellent tools for Galactic Plane investigations.

About 90% of SNRs and SNR candidates have been found in radio surveys (Anderson, et al. 2017), but it is thought that there could be many missing SNRs (e.g. Li et al. 1991; Tammann et al. 1994; Gerbrandt et al. 2014). Obtaining a more complete record of the SNR population, including confirming or rejecting the nature of SNR candidates, is important as it leads to better estimates of the Galactic supernova rate, the maximum ages of SNRs, and because SNRs are obvious locations for searching for young pulsars.

Low-frequency ($\lesssim 350$ MHz) Galactic Plane observations are useful for investigating SNRs and SNR candidates, particularly for differentiating between SNR candidates and HII regions, due to the typically steeper radio spectral indices of SNRs ($\alpha \approx -0.5$; Onić 2013) as compared to HII regions ($\alpha \gtrsim 0$); where $S_\nu \propto \nu^\alpha$ for S_ν integrated flux density in Jy and ν frequency in Hz (Onić 2013). This means that SNRs are brighter at lower frequencies, while HII regions are brighter at higher frequencies. However, there have been relatively few low-frequency surveys of the Galactic Plane with high angular resolution and sensitivity. A good illustration of the capability of such surveys for SNR searches was demonstrated by a 333 MHz survey with the Very Large Array (VLA) of the Galactic Center region (Brogan et al. 2006). This survey resulted in the discovery of 35 new candidate SNRs, 31 of which are now confirmed. Multi-wavelength analysis is required to confirm (or reject) SNR candidates, such as X-ray observations

or further radio observations at a different frequency to confirm the spectral index.

The LOw-Frequency ARray (LOFAR; van Haarlem et al. 2013) is an interferometer that observes at low-frequencies with a large field-of-view (FoV; e.g. ~ 11 deg² using HBA Dual Inner mode), which means that it is ideal for observing and discovering steep-spectra objects and for differentiating between SNR candidates and HII regions. LOFAR consists of two arrays: the Low Band Antennas (LBA) and the High Band Antennas (HBA). The LBA observes between 10 and 80 MHz while the HBA observes between 110 and 250 MHz. The wide FoV also introduces many technical difficulties regarding calibration and imaging, particularly as the ionosphere can introduce significant phase and amplitude variations across the FoV.

Here we discuss six SNR candidates in the FoV of proprietary LOFAR HBA observations (PI: J. D. Gelfand) that overlap with an archival Westerbork Synthesis Radio Telescope (WSRT) mosaic (Taylor et al. 1996) and an archival VLA Galactic Plane Survey (VGPS) mosaic (Stil et al. 2006). These SNR candidates were identified in a study of THOR+VGPS observations by Anderson, et al. (2017) and are: G51.21 + 0.11, G52.37 – 0.70, G53.07 + 0.49, G53.41 + 0.03, G53.84 – 0.75, and G54.1 + 0.3. In particular, we present a multi-frequency analysis of SNR candidate G53.41 + 0.03. In Section 2 we present the observations. In Section 3 we present our results and in Section 4 we discuss the SNR candidates. We conclude in Section 5.

2. OBSERVATIONS AND ANALYSIS

2.1. Radio observations

We use radio observations at three different frequencies – 144 MHz (LOFAR HBA), 327 MHz (WSRT), and 1400 MHz (VGPS) – to investigate part of the Galactic Plane. Figure 1 shows the FoV where our LOFAR HBA observations overlap archival WSRT and VGPS mosaics.

We initially obtained and analyzed the LOFAR observations to investigate pulsar wind nebula (PWN) G54.1 + 0.3 but, due to the large FoV, we also investigated other promising SNR candidates. The LOFAR observations are centered on the PWN. The observations were taken on 2015 June 12 as part of project LC4.011 (ObsID: 345918) and were performed in HBA Dual Inner mode (van Haarlem et al. 2013). This means that the inner 24 tiles of the remote stations were used resulting in a full-width half-maximum (FWHM) of the primary beam of 3.8° and FoV of ~ 11 deg² in this configuration. The LOFAR HBA target and calibrator scans cover the frequency range from 118.7 MHz to 169.5 MHz. The observing bandwidth was split into 260 subbands (SBs)

¹ www.astro.phys.wvu.edu/wise

with bandwidth of 195.3 kHz each. For these observations an 18 min calibrator scan of 3C380 was taken before and after the 3 hr target scan.

The LOFAR observations were flagged, demixed, and averaged as part of standard LOFAR pre-processing. Demixing involves removing the effects of the very bright radio sources, Cassiopeia A and Cygnus A, that affect LOFAR images even when they are far from the phase center of the FoV. The data were averaged to 4 frequency channels per SB. The LOFAR synthesized beam size is $3.0' \times 2.2'$ with a position angle of 220.7° (with respect to the Galactic Plane) at 144 MHz using a Briggs weighting of 1.0 (Briggs 1995). As this is a Galactic Plane observation the imaging calibration pipeline, prefactor (or Pre-Facet-Cal; van Weeren et al. 2016), was not successful. This is due to the significant extended emission in the Galactic Plane, across the FoV. Ionospheric variations during the observations were particularly pronounced. The observation was calibrated by transferring the time-independent, zero-phase gain solutions from the second calibrator scan to the target scan. The observations were then summed into 26 measurement sets of 10 SBs each. Two rounds of self-calibration were then performed on the target scan, the first using a model from the TIFR GMRT Sky Survey (TGSS) Alternative Data Release (TGSS ADR², Intema et al. 2017). Multiscale imaging with Briggs 1.0 weighting was then performed using the WSClean tool (Offringa et al. 2014). The subband with a central frequency of 150 MHz was flux calibrated using the integrated flux density measurements of point sources from the TGSS ADR. It is important to note that the sensitivity of the LOFAR image drops significantly at the edge of the FWHM of the primary beam. This means that flux density values far from the phase center (PWN G54.1 + 0.3) are less reliable. Figure 1 was produced by performing a multi-frequency (MFS) clean on all measurement sets.

WSRT observations were obtained from a Galactic Plane point source survey at 327 MHz with a beam size of $60'' \times 191''$ and a position angle of 61.3° (with respect to the Galactic Plane) by Taylor et al. (1996)³. VLA observations from VGPS with a beam size of $1' \times 1'$ were also used (Stil et al. 2006)⁴. The VLA observations have the highest angular resolution of the available radio observations of this FoV.

2.2. Radio pulse search observations

² <http://tgssadr.strw.leidenuniv.nl/doku.php>

³ www.ras.ualgary.ca/wsrt_survey.html

⁴ www.ras.ualgary.ca/VGPS/VGPS_data.html

To search for a pulsar towards G53.41 + 0.03, we observed the region using the 305-m Arecibo radio telescope and the 7-beam Arecibo L-band Feed Array (ALFA) receiver. On 2017 June 21, we made a 3-pointing grid of the region, where together the 21 observed beams were interleaved and cover a roughly $10'$ region around the center of G53.41 + 0.03. The first pointing, where the central beam of ALFA was directly pointed towards the apparent center of G53.41+0.03, integrated for 2400 s. The other two interleaving pointings were integrated for 900 s. We recorded the resulting filterbank data using the Mock spectrometers, which provided two partially overlapping 172 MHz subbands centered at 1300 and 1450 MHz, respectively. Only total intensity was recorded, with 0.34-MHz spectral channels and $65.5 \mu\text{s}$ time resolution. We converted the raw samples from 16-bit to 4-bit values subsequent to the observation in order to reduce the data volume. At the start of the session, we observed PSR J1928+1746 in the central ALFA beam, in order to verify the configuration.

We searched for radio pulsations in the direction of G53.41 + 0.03 using standard methods, as implemented in the PRESTO⁵ software package. We chose to search the Mock subbands separately because the lower-frequency subband contains significantly more radio frequency interference (RFI). For each beam and subband we excised RFI using `rfifind` and then used multiple calls to `prepsubband` to generate dedispersed time series for dispersion measures in the range $\text{DM} = 0 - 1019 \text{ pc cm}^{-3}$ in steps of 1 pc cm^{-3} . The remaining dispersive smearing is $\sim 1 \text{ ms}$, even for the highest DMs in this range. Each dedispersed timeseries was then searched for periodicities using `accelsearch` with no additional search for linear acceleration (i.e. $z_{\text{max}} = 0$). The cumulative set of candidates was then sifted and ranked using `ACCEL_sift.py`. We folded promising candidates — those with high signal-to-noise, high coherent power, and apparent peaks in signal-to-noise as a function of DM — using `prepfold`. Associated diagnostic plots for each candidate were then visually inspected. When this approach was applied to the test pulsar, J1928+1746, the expected signal was easily recovered in both subbands.

2.3. Infrared observations

The FoV coinciding with the radio observations was observed at $24.0 \mu\text{m}$ as part of the Multiband Infrared Photometer for Spitzer GALactic Plane (MIPSGAL) survey (Carey et al. 2009; Gutermuth & Heyer 2015).

⁵ <https://github.com/scottransom/presto>

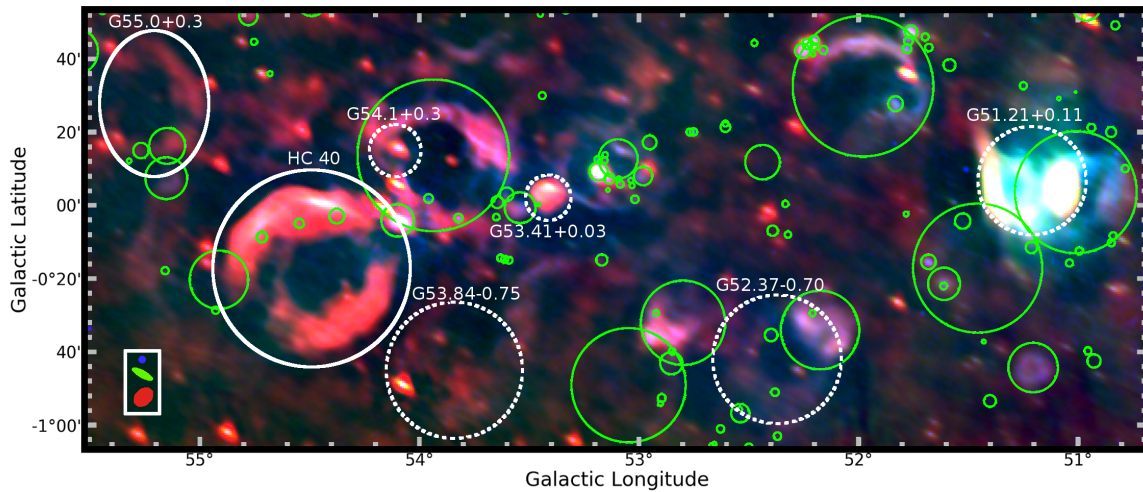


Figure 1. Observations of the Galactic Plane at 1.4 GHz (blue, VLA), 327 MHz (green, WSRT), and 144 MHz (red, LOFAR HBA). The synthesized beam sizes are shown in the bottom left corner. Known SNRs from Green’s SNR catalog (Green 2014) are circled in solid white and candidate SNRs from Anderson, et al. (2017) are circled in dashed white. The green circles are HII regions from the WISE catalog (Anderson et al. 2014).

MIPSGAL $24.0\ \mu\text{m}$ observations have a resolution of $6''$ and a 5σ root-mean-squared sensitivity of $1.3\ \text{mJy}$.

2.4. X-ray observations

Of the six candidate SNRs that we investigate in this paper, only the possible shell around PWN G54.1 + 0.3 has been analysed previously in the X-ray band. It has been observed using *Chandra* (Lu et al. 2002), *Suzaku*, and *XMM-Newton* (Bocchino et al. 2010).

The position of G53.84 – 0.75 has been observed in a *ROSAT* PSPC observation (ObsID: WG500209P.N1). Using the region size of $18.7'$ (Anderson, et al. 2017) we estimate the X-ray count rate with 2σ upper limit to be 1.5×10^{-2} counts/sec in the *ROSAT* 0.4 – 2.4 keV energy band.

G53.41+0.03 is detected at the edge of the FoV of two *ROSAT* PSPC observations (ObsIDs: WG500042P.N2 and WG500209P.N1) and partially covered by an *XMM-Newton* observation taken on 2008 Mar 29 (ObsID: 0503740101). The other three SNR candidates, G51.21+0.11, G52.37 – 0.70, and G53.07 + 0.49, have no complementary data available in the X-ray band.

Although G53.41 + 0.03 lies at the edge of the detector in the *XMM-Newton* observation, the observation is important as it allows us to determine the nature of the X-ray emission through spectral analysis of the EPIC-MOS camera (Turner et al. 2001) data. We extracted the spectrum with the Science Analysis System (SAS) v14.0. Due to a failed CCD chip in MOS1 and the smaller FoV of the EPIC-PN detector only data from the MOS2 detector were used. The data were reduced using the `emproc` task and filtered for the background flaring. This resulted in 40.7 ks of cleaned exposure time. The

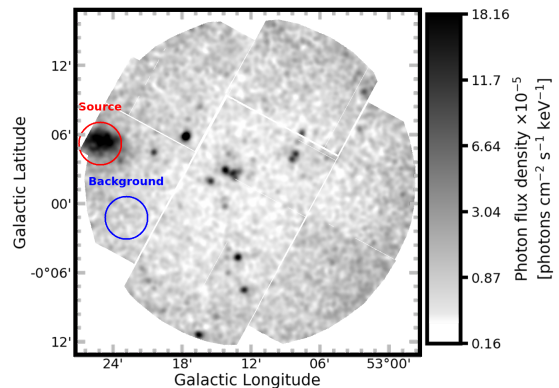


Figure 2. Exposure and vignetting corrected image from the *XMM-Newton* MOS2 detector. Source and background extraction regions are circled.

source extraction region was a $1.8'$ radius circle centered on the extended X-ray source. The background was extracted using a region of the same size positioned in a nearby area of the detector devoid of X-ray sources. The source and background regions are shown in Figure 2.

To perform the spectral analysis the SPEX fitting package version 3.04 (2017) together with SPEXACT 2.07 atomic tables were used (Kaastra et al. 1996). The fitting statistics method employed was C-statistics (Cash 1979). Abundances were expressed with respect to Solar Abundance values of Lodders et al. (2009). For the emission measure parameter ($n_e n_H V$) we assumed a distance of 7.5 kpc (see Sec. 4.1). The analysis of the spectra was performed in the energy range between 0.7 – 3.0 keV, as this is the range in which the source spectrum dominates the background. The `Obin` command was used to obtain optimal binning of the spectra. Af-

ter background subtraction the source spectrum consists of ~ 2000 counts. The spectrum was fit with a non-equilibrium ionization (NEI) model with Galactic absorption. The Galactic background was represented by the model `hot` in SPEX, with the temperature fixed to 0.5 eV to mimic absorption by neutral gas (de Plaa et al. 2016). The NEI model was employed with the following free parameters: electron temperature T_2 , ionization age $\tau = n_e t$, normalization $n_e n_H V$, and abundances of elements Ne, Mg, Si, S, Fe. These elements have line emission in the energy band from 0.8 – 2.6 keV, the band for which there was sufficient signal to noise.

2.5. High-energy observations

We searched the High Energy Stereoscopic System CAtalog (HESSCAT⁶) and Third *Fermi* LAT CAtalog of High-Energy Sources (3FGL; Acero et al. 2015) for high-energy sources associated with any of the SNR candidate shells. *Fermi* source 3FGL J1931.1+1659 is within the radius of SNR candidate G52.37 – 0.70. There are no other high-energy sources close to the other five SNR candidates.

3. RESULTS

The VGPS, WSRT, and LOFAR HBA observations of the six SNR candidates in the FoV – G51.21 + 0.11, G52.37 – 0.70, G53.07 + 0.49, G53.41 + 0.03, G53.84 – 0.75, and G54.1 + 0.3 – are shown in Figures 3 and 4. Only G53.41+0.03 and G54.1+0.3 have been observed in the X-ray band (see Sec. 2.4). As discussed by Anderson, et al. (2017), all six of the candidates have low thermal emission compared to the non-thermal emission, which we confirm using the MIPS GAL observations.

3.1. Radio results

The flux densities and spectral indices of SNR candidates G51.21 + 0.11, G52.37 – 0.70, G53.41 + 0.03, and G53.84 – 0.75, and the candidate shell around PWN G54.1 + 0.3 measured using the positions and radii reported by Anderson, et al. (2017) are shown in Table 1. We subtracted the integrated flux density of the HII region overlapping G52.37 – 0.70 and the flux density of the bright point source within G53.84 – 0.75. Due to a drop-off in sensitivity away from the phase center of the HBA observation, we do not measure LOFAR integrated flux densities for G51.21 + 0.11 and G52.37 – 0.70.

SNR candidate G51.21 + 0.11, shown in Figure 3 (top row), has a complex morphology with a bright radio filament type structure and a bright radio patch. It has

an HII region, G051.010+00.060 (Anderson et al. 2014), on one side that appears to be coincident.

G52.37 – 0.70 is a faint radio shell visible most clearly in the VLA observation in the second row of Figure 3. There is a bright HII region, G052.174 – 00.567 (Anderson et al. 2014), on the upper right of this candidate and some smaller HII regions within the shell.

G53.07 + 0.49 has a small angular size (a radius of only $1'$, Anderson, et al. 2017) and the location of the peak flux density is different for WSRT and LOFAR compared to the original VLA identification of the candidate. In Figure 3 (bottom panel) we can also see that there is some extended emission around G53.07 + 0.49 that may or may not be associated with this candidate. As it is unclear which emission in the WSRT and LOFAR observations may or may not be associated with the candidate we do not measure WSRT or LOFAR flux densities for this candidate.

There is diffuse emission and some radio point sources in the region where candidate G53.84 – 0.75 is located (Fig. 4, upper panel), but it is difficult to identify what emission is related to candidate G53.84 – 0.75 and whether there is a discrete object or if the extended emission is Galactic Plane dust.

PWN G54.1 + 0.3 is shown in Figure 4 (lower panel) where the bright spot in the center is the PWN and the partial loop around it is the known HII region G053.935+00.228 (Anderson et al. 2014). There is some faint, diffuse radio emission around the PWN in the VLA observation, which is the SNR-shell candidate. In the WSRT and LOFAR observations of PWN G54.1+0.3 shown in Figure 4 it appears that the possible shell identified in the VLA observations (Anderson, et al. 2017) fades away or is part of the surrounding HII region. The large uncertainty in the spectral index in Table 1 reflects that a powerlaw is not the best model; however, the flux density clearly decreases as the frequency decreases.

In the LOFAR HBA and VLA observations G53.41 + 0.03 has a shell- or bubble-like morphology which is brighter on the upper edge, as shown in Figure 5. The radius of the shell at 144 MHz is $\sim 5'$. As shown in Table 1 G53.41 + 0.03 has a radio spectral index of $\alpha = -0.6 \pm 0.2$.

3.2. X-ray results

As described in Sec. 2.4, G53.84 – 0.75 was observed by *ROSAT*. We used the PIMMS⁷ tool with the optically thin plasma model APEC with temperature 0.3 keV and local Galactic absorption value of $2.4 \times 10^{22} \text{ cm}^{-2}$ to

⁶ www.mpi-hd.mpg.de/hfm/HESS/pages/home/sources/

⁷ <https://heasarc.gsfc.nasa.gov/cgi-bin/Tools/w3pimms/w3pimms.pl>

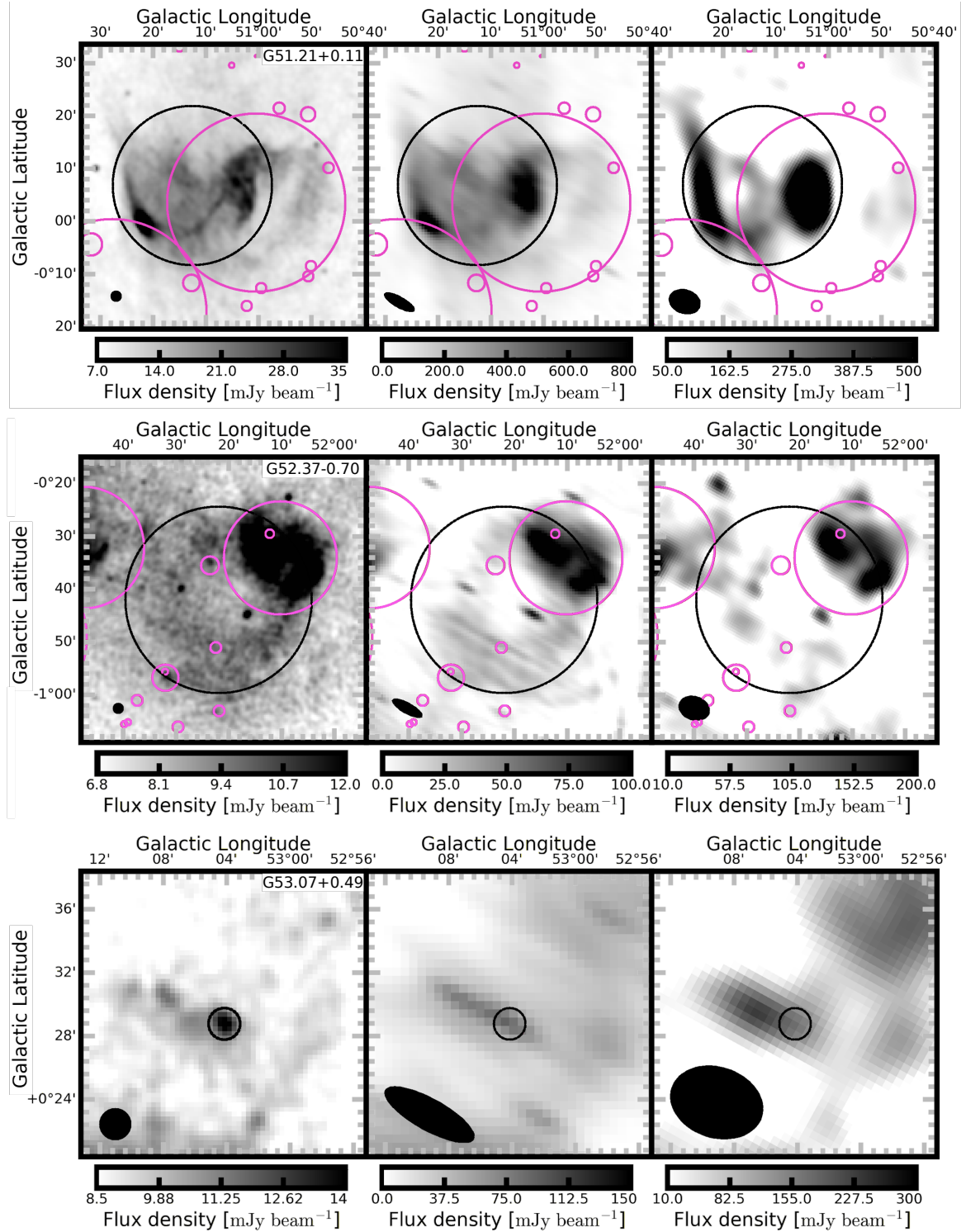


Figure 3. SNR candidates from Anderson, et al. (2017) in the FoV. In each row the left panel is the VGPS 1.4 GHz observation, the center panel is the WSRT 327 MHz observation, and the right panel is the LOFAR 144 MHz observation. From top to bottom the rows are the SNR candidates (circled in black) from Anderson, et al. (2017): G51.21+0.11, G52.37-0.70, and G53.07+0.49. The magenta circles are HII regions from the WISE HII catalog (Anderson et al. 2014). The beam sizes are shown in the bottom left corner of each panel.

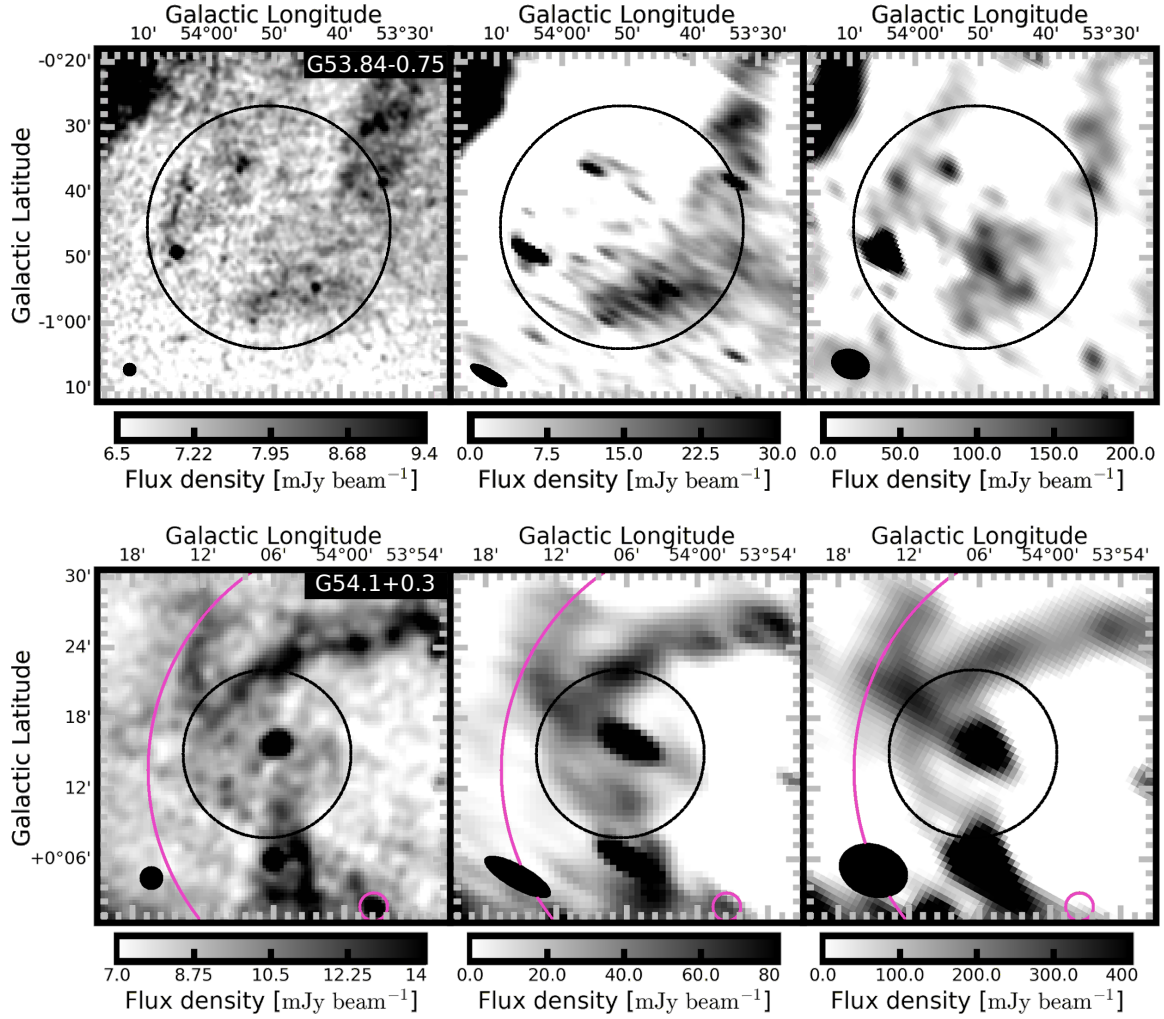


Figure 4. SNR candidates from Anderson, et al. (2017) in the FoV. In each row the left panel is the VGPS 1.4 GHz observation, the center panel is the WSRT 327 MHz observation, and the right panel is the LOFAR 144 MHz observation. From top to bottom the rows are the SNR candidates (circled in black) from Anderson, et al. (2017): G53.84 – 0.75 and G54.1 + 0.3. The magenta circles are HII regions from the WISE HII catalog (Anderson et al. 2014). The beam sizes are shown in the bottom left corner of each panel.

SNR	Flux density (Jy)			α
	1.4 GHz	327 MHz	150 MHz	
G51.21+0.11	24.35 ± 2.1	66.1 ± 0.1		-0.7 ± 0.21
G52.37–0.70	5.24 ± 1.75	3.2 ± 0.03		0.3 ± 0.3
G53.41+0.03	1.21 ± 0.21	2.2 ± 0.03	3.11 ± 0.2	-0.6 ± 0.2
G53.84–0.75	1.31 ± 3.43	0.06 ± 0.02	1.2 ± 0.07	0.05 ± 3.9
G54.1+0.3	1.46 ± 0.28	1.21 ± 0.05	0.4 ± 0.8	0.3 ± 4.3

Table 1. Integrated flux densities of SNR candidates at 1.4 GHz from Anderson, et al. (2017), 327 MHz measured using WSRT observations (Taylor et al. 1996), and 150 MHz using LOFAR HBA observations. The WSRT errors are 3σ statistical errors based on the RMS noise in the image; these errors do not take other sources of error, such as confusion, into account. α was obtained using a simple power law and a weighted least squares fit using the measured error plus 20% for systematics. We note that a simple power law is not always the best model, for example for G54.1 + 0.3.

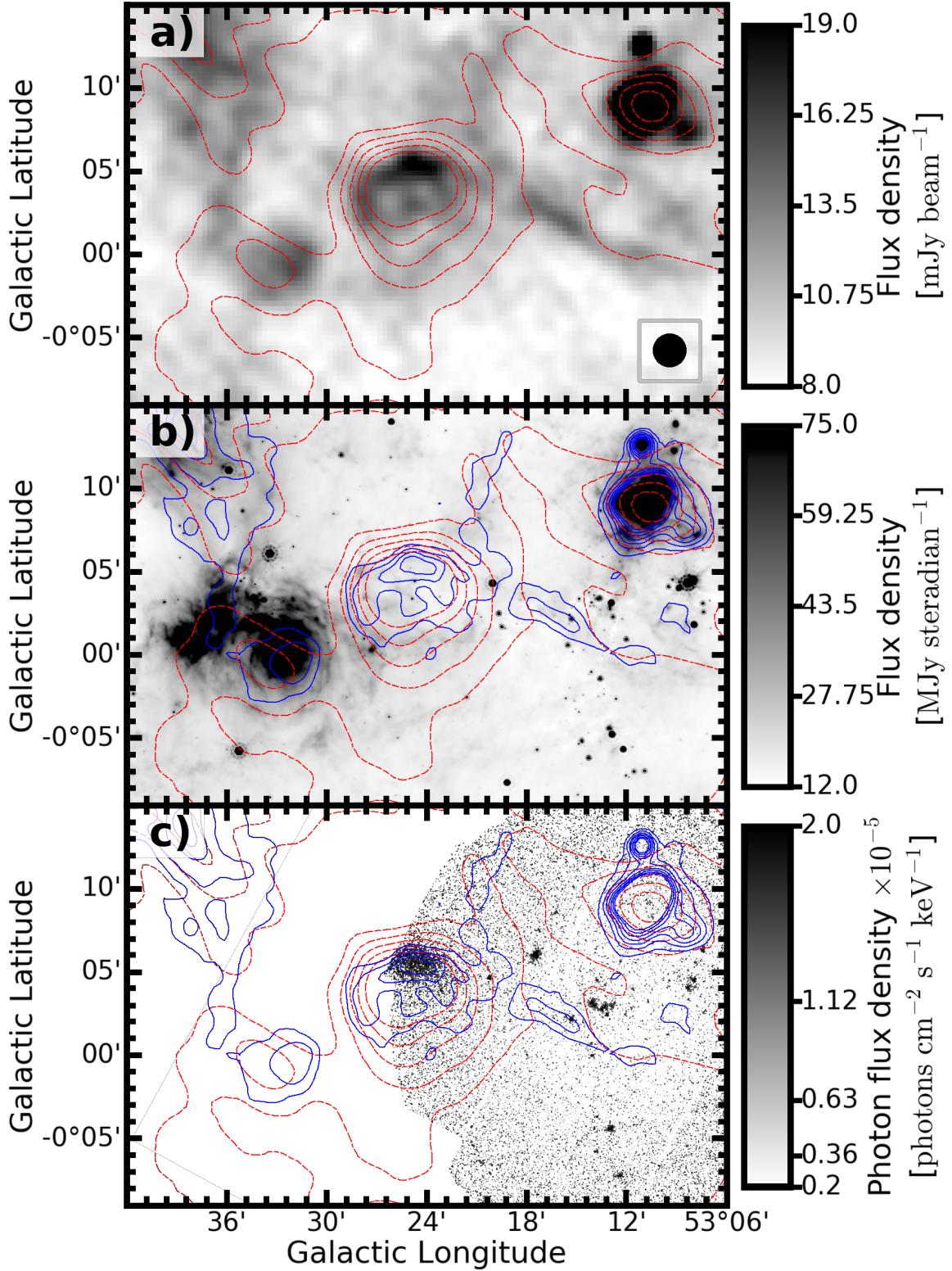


Figure 5. Observations of G53.41 + 0.03 at (a) 1.4 GHz using the VLA, (b) 24.0 μm using *Spitzer*, and (c) X-rays using *XMM-Newton*. The dashed red contours are LOFAR HBA 144 MHz contours (contour levels: 0, 250, 500, 750, 1000 mJy beam^{-1}) and the solid blue contours are VLA 1.4 GHz contours (contour levels: 12, 14, 16, 18, 20, 22, 24 mJy beam^{-1}) from the image in (a). The VLA synthesised beam is shown in the bottom right corner of (a).

Parameter	Unit	Value	Element	Abundance
N_H	10^{22} cm^{-2}	$2.4^{+0.2}_{-0.2}$	Ne	$0.2^{+0.7}_{-0.2}$
$n_e n_H V$	10^{57} cm^{-3}	5^{+2}_{-2}	Mg	$0.9^{+0.3}_{-0.2}$
T_2	keV	$0.8^{+0.2}_{-0.1}$	Si	$0.5^{+0.1}_{-0.1}$
τ	$10^{10} \text{ s cm}^{-2}$	4^{+2}_{-1}	S	$0.9^{+0.2}_{-0.2}$
			Fe	$1.3^{+0.7}_{-0.5}$
Cstat/d.o.f				83.48/64

Table 2. *XMM-Newton* best-fit model results. The abundances are provided in Solar units.

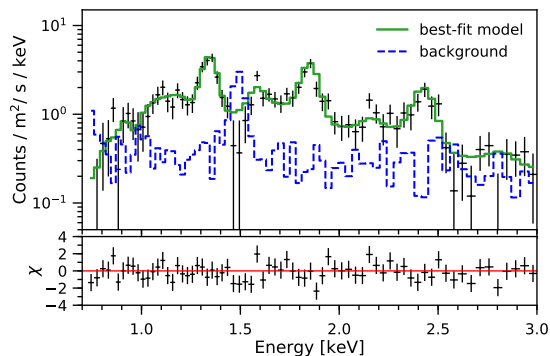


Figure 6. X-ray spectrum with the best-fit model and residuals.

obtain the 2σ upper limit for the flux. No X-ray feature coincident to the radio observations was detected. The 2σ upper limit for the absorbed/unabsorbed flux is $F_{0.4-2.4} \approx 2.4 \times 10^{-13} / 4.1 \times 10^{-11} \text{ erg s}^{-1} \text{ cm}^{-2}$.

The *ROSAT* and *XMM-Newton* X-ray observations of G53.41+0.03 confirm the existence of an extended X-ray source at the location of G53.41 + 0.03, particularly at the position of the radio-bright part of the shell⁸. The *XMM-Newton* X-ray spectrum (Fig. 6) shows bright K-shell emission lines from magnesium, silicon, and sulfur and potential contributions from neon and iron around 1 keV. This is typical of thermal emission from an optically thin plasma. The absorbed/unabsorbed flux of the source measured using *XMM-Newton* in the 0.7 – 3.0 keV energy range is $F = 7.3 \times 10^{-13} / 3.1 \times 10^{-11} \text{ erg s}^{-1} \text{ cm}^{-2}$. The best-fit NEI model is represented by a C-stat / d.o.f. of 83.48/64. The parameters and 1σ errors are listed in Table 2, while the best fit model is shown in Figure 6. The ionization age informs us how far out of ionization equilibrium the plasma is, but given

⁸ Since the spectral resolution of the *ROSAT* PSPC is poor and the images are noisy, we use only the *XMM-Newton* observation for further analysis.

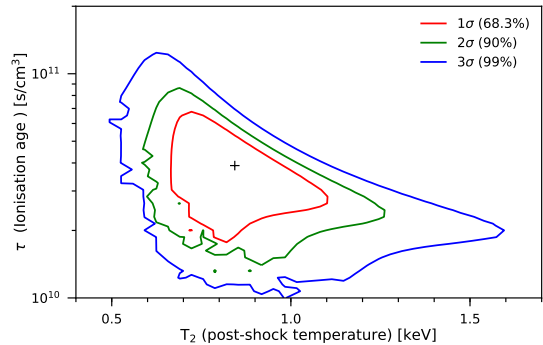


Figure 7. Contour plot of the ionization age and post-shock temperature. Best fit values are indicated by a small cross.

the narrow spectral range the parameter may correlate with the best-fit electron temperature T_2 . To test the robustness of our best fit ionization age we calculate the error ellipse of τ and T_2 , as shown in Figure 7.

3.3. Radio pulsation search results

After performing a pulsation search as described in Sec. 2.2 we found no convincing astronomical signals in the data toward G53.41 + 0.03, and we ascribe the statistically significant signals that we did detect to RFI.

Given the non-detection of radio pulsations toward G53.41 + 0.03, we can place an upper limit on the integrated flux density of any associated radio pulsar. We use the modified radiometer equation (Dewey et al. 1985), and assume that interstellar scattering does not have a significant effect on broadening the pulses through multi-path propagation. While the central ALFA beam has a gain of $G \sim 10 \text{ K Jy}^{-1}$, the 6 outer beams have $G \sim 8 \text{ K Jy}^{-1}$. We targeted the center of G53.41 + 0.03 (specifically, $\text{RA}_{\text{J2000}} = 19^{\text{h}}29^{\text{m}}57.41^{\text{s}}$, $\text{Dec}_{\text{J2000}} = +18^{\circ}09'53.5''$) in a $T = 2400$ -s pointing with the central ALFA beam, which covered a region of roughly $1.6'$ in radius. Since G53.41 + 0.03 is roughly $10'$ wide, we also gridded a much larger $\sim 10'$ wide region around G53.41 + 0.03 in case the pulsar has moved from its birth site near the center of the SNR. In our sensitivity calculations we thus consider two scenarios: 1) where the pulsar is close to the center of G53.41 + 0.03, and where we should use $G = 10 \text{ K Jy}^{-1}$ and $T = 2400$ s and 2) a scenario in which the pulsar is offset by several arcminutes, and where $G = 8 \text{ K Jy}^{-1}$ and $T = 900$ s. Furthermore, if the pulsar is located towards the half-power sensitivity point of one of the beams, then the effective sensitivity is also half. We make this conservative assumption for scenario 2.

The receiver temperature $T_{\text{rec}} = 25 \text{ K}$ and the sky temperature in this direction of the Galactic plane is $T_{\text{sky}} = 5 \text{ K}$ at 1400 MHz. We assume a $W = 10\%$ pulse

duty cycle and a signal-to-noise $S/N = 10$ for detection. The two orthogonal linear polarizations, n_p , of the receiver were summed, and the appropriate bandwidth is $\Delta\nu = 172$ MHz. Finally, using the modified radiometer equation, and assuming no additional losses due to digitization, we find for scenario 1:

$$S_{\max}^1[\text{mJy}] \frac{S/N(T_{\text{rec}} + T_{\text{sky}})}{G\sqrt{T\Delta\nu n_p}} \sqrt{\frac{W}{(1-W)}} = 0.011 \text{ mJy} \quad (1)$$

For scenario 2, where the putative pulsar is more offset from G53.41 + 0.03, $S_{\max}^2 = 0.045$ mJy. These are deep upper-limits on the flux density of any pulsar associated with G53.41 + 0.03. Of the known young pulsars in the ATNF catalog, only a few have lower measured radio flux density (Manchester et al. 2005). However, because of beaming and the possibility of significant interstellar scattering, these limits do not definitively exclude a young pulsar associated with G53.41 + 0.03.

4. DISCUSSION

Here we will discuss the characteristics and nature of each SNR candidate. We will focus on G53.41 + 0.03, including calculating its approximate distance and age.

G51.21+0.11: SNR candidate G51.21 + 0.11 has a negative spectral index, $\alpha = -0.7 \pm 0.21$, and a complex morphology coincident with a known HII region. There are no *XMM-Newton* or *Chandra* observations in the direction of the candidate to confirm its nature. We find G51.21 + 0.11 to be an interesting object that is possibly an SNR, but further investigation using X-ray observations is required.

G52.37–0.70: Although G52.37 – 0.70 has a shell-like morphology in the VLA observations, it has a spectral index of $\alpha = 0.3 \pm 0.3$ fitted using the VLA and WSRT integrated flux densities. The spectral index indicates that this candidate is unlikely to be an SNR, and as such the *Fermi* source within the radius of the candidate (see Sec. 2.5) is unlikely to be associated.

G53.07+0.49: Candidate G53.07 + 0.49 has a small angular size in the VLA observations, but the peak flux density in the WSRT and LOFAR observations is offset from the SNR candidate location suggested by (Anderson, et al. 2017). As such we do not measure WSRT or LOFAR flux densities for this candidate, and as there are no X-ray observations available, further investigation using X-ray or higher resolution low-frequency observations is required to comment on the nature of this candidate.

G53.84–0.75: It is not clear what emission is SNR candidate G53.84 – 0.75 and there are large errors on the VLA integrated flux density from Anderson, et al.

(2017). This, as well as the strange spectral shape, suggests that there is no discrete, extended object at this position. This is supported by the *ROSAT* X-ray non-detection. For this reason we find it unlikely that G53.84 – 0.75 is an SNR.

G54.1+0.3: Whether PWN G54.1 + 0.3 has an SNR shell has been in question since Lang et al. (2010) found faint radio emission around the PWN, which is just visible in the VLA observation (Fig. 4). Lu et al. (2002) found no evidence of a shell in their *Chandra* observations, while Bocchino et al. (2010) found hints of a very faint, diffuse shell using *Suzaku* and *XMM-Newton*. Anderson, et al. (2017) find that the shell suggested by Lang et al. (2010) is more likely to be part of the surrounding HII region. Alternatively, Anderson, et al. (2017) suggest a slightly smaller radius shell ($7.2'$) as a possible shell around PWN G54.1 + 0.3 with an integrated flux density of 1.46 Jy at 1.4 GHz. There is no evidence for extended emission around PWN G54.1+0.3 in our LOFAR HBA observation, as can be seen in Figure 4 (bottom panel), aside from the known HII region G053.935 + 0.228 (Anderson et al. 2014). This is supported by the low flux-densities measured by WSRT and LOFAR (shown in Table 1) using a region of radius $7.2'$ and subtracting the flux density of the PWN. We find it unlikely that there is a shell around PWN G54.1 + 0.3.

G53.41+0.03: G53.41 + 0.03 has a morphology common to SNRs. Using the flux densities shown in Table 1 we find that the G53.41 + 0.03 has a steep negative radio spectral index, $\alpha = -0.6 \pm 0.2$, as expected for an SNR. X-ray analysis indicates that the plasma of G53.41 + 0.03 has a relatively high temperature of $T_2 \sim 0.8$ keV. The ionization age $\tau \sim 10^{10.6} \text{ s} \cdot \text{cm}^{-3}$ is much lower than needed for ionization/recombination balance ($\tau \geq 10^{12} \text{ s} \cdot \text{cm}^{-3}$). The fact that the spectrum is far out of ionization equilibrium is a clear signature that the source is an SNR (Vink 2012), as no other known source class has gas tenuous enough and/or is young enough to be far out of ionization equilibrium. We therefore confirm that G53.41 + 0.03 is an SNR, and further investigate it by calculating its approximate distance and age.

4.1. The distance to G53.41+0.03

Estimating the distance to Galactic SNRs is notoriously difficult. There are few methods that give reliable results, such as kinematic methods, based on optical Doppler shifts combined with proper motion of optical filaments (e.g. Reed et al. 1995, for Cas A), or, less reliably, 21cm line absorption combined with a Galactic rotation model (see e.g. Roman-Duval et al. 2009; Kothes & Foster 2012, for an explanation and SNR ap-

plication of the model). In contrast, SNRs located in the Magellanic Clouds can be reliably placed at the distance of these satellite galaxies. By using reliable distance estimates some secondary distance indicators have been developed, such as the X-ray Galactic absorption column (Strom 1994) and the $\Sigma - D$ relation (Pavlovic et al. 2014).

A first indication of the distance of an SNR can be its positional association with a spiral arm. However, the reason that the investigated field is so rich in sources is that the line of sight crosses the Sagittarius-Carina arm tangentially as well as regions of the Perseus arm. Taking the Galactic spiral arm model of Hou et al. (2009), we find that the $l = 53.4^\circ$ line of sight intercepts the Sagittarius arm (arm -3 in Hou et al. 2009) between ~ 4 kpc and 7.5 kpc, and the Perseus arm at 9.6 kpc. Given that the Sagittarius arm is tangential along the line of sight, this suggests a probable distance between 4.5 and 7.5 kpc.

Strom (1994) derived a relation between column density and distance of $N_H = 8.4 \times 10^{21} d^{1.58} \text{ cm}^{-2}$. The measured column density of $N_H = 2.4 \times 10^{22} \text{ cm}^{-2}$ (Table 2), therefore, suggests a distance of ~ 8.4 kpc. However, one should be cautious here, because the line of sight crosses the arm tangentially, which is likely to lead to a column density that is higher than average for a given distance.

The surface brightness of G53.41+0.03 normalized to 1 GHz is $\Sigma = 8.3 \times 10^{-21} \text{ W m}^{-2} \text{ Hz}^{-1} \text{ sr}^{-1}$. The 1 GHz surface brightness was obtained using the 1.4 GHz flux density measured by Anderson, et al. (2017) and a spectral index of $\alpha = -0.6$ (see Tab. 1). Using the relation between diameter and surface brightness (the $\Sigma - D$ relation) in Pavlovic et al. (2014) gives yet another distance estimate of 8 kpc. However, we know that the $\Sigma - D$ relation is controversial, as there is large scatter which may relate to the SNR environments, and there is debate on the statistical validity of the relation (e.g. Arbutina & Urošević 2005; Filipović et al. 2005; Green 2014).

The distance estimates based on the X-ray absorption and $\Sigma - D$ relation, although uncertain, are consistent with the idea that the SNR is located in the Sagittarius-Carina arm, but suggest that the SNR is on the far-side of the arm. We therefore adopt a distance of 7.5 kpc for G53.41+0.03. The angular radius of $\sim 5'$ translates then into a physical radius of $10.7 d_{7.5} \text{ pc}$, with $d_{7.5}$ the distance in units of 7.5 kpc.

4.2. The age of G53.41+0.03

The spectrum of G53.41+0.03 allows us to put some constraints on the density and age of the SNR. To do

this we need a volume estimate. Given a typical volume filling fraction of 25%⁹ and assuming a spherical morphology, we estimate the volume to be $V_{\text{SNR}} = 3.3 \times 10^{58} d_{7.5}^3 \text{ cm}^3$. The X-ray spectrum was obtained for only $\sim 20\%$ of the shell, so we take $V_X \approx 6.7 \times 10^{57} d_{7.5}^3 \text{ cm}^3$ to be the volume pertaining to the X-ray spectrum. Taking $n_e \approx 1.2 n_H$ in the emission measure $n_e n_H V$, we obtain the density $n_H \approx 0.8 d_{7.5}^{-3/2} \text{ cm}^{-3}$. Using this number together with the best-fit ionization age of $n_e t = 4 \times 10^{10} \text{ cm}^{-3} \text{ s}$ we find an approximate age of $1600 d_{7.5}^{3/2} \text{ yr}$.

The measured electron temperature corresponds to a shock velocity of $V_s \approx 800 \text{ km s}^{-1}$ or higher if the electron temperature is lower than the ion temperature (Vink 2012). For the Sedov-Taylor self-similar evolution model we have $V_s = 0.4R/t$. Using $R = 10.7 d_{7.5} \text{ pc}$, gives then an approximate age of $\sim 5300 d_{7.5} \text{ yr}$. Using the Sedov-Taylor evolution model of $R^5 = 2.026 E t^2 / \rho$, with $E = 10^{51} \text{ erg}$ gives yet another estimate of the age of $\sim 7800 d_{7.5}^{7/4} \text{ yr}$. The two estimates based on the Sedov-Taylor model give roughly similar results for the canonical explosion energy of 10^{51} erg ($t \approx 6500 \pm 1500 \text{ yr}$), whereas the estimate based on the ionization age suggests a younger age. This discrepancy may be due to non-standard evolution scenarios, for example evolution in a wind-blow cavity. This needs to be addressed in follow-up studies. However, these estimates agree that G53.41+0.03 is an SNR with an age somewhere between 1000 and 8000 yr. X-ray observations centered on and covering the whole SNR are needed to fully characterize the properties of G53.41+0.03.

5. CONCLUSION

We confirm that SNR candidate, G53.41+0.03, is in fact an SNR using *XMM-Newton* observations, and LOFAR observations targeting PWN G54.1+0.3. G53.41+0.03 has a shell-like morphology in the radio, with a radius of $\sim 5'$. Using LOFAR HBA observations, as well as archival WSRT and VGPS mosaics, we confirm that G53.41+0.03 has a steep spectral index ($\alpha = -0.6 \pm 0.2$), typical of synchrotron radiation from SNRs. MIPS GAL observations show that G53.41+0.03 has no IR component. Archival *XMM-Newton* observations show that G53.41+0.03 has an associated X-ray component with a coincident morphology to the radio shell. Furthermore, analysis and fitting of the *XMM-Newton* observation show that G53.41+0.03 has strong emission lines and is best characterized by a non-equilibrium ioniza-

⁹ A strong shock has a compression factor of 4. This means that roughly 25% of the volume, approximated by a sphere, will emit.

tion model, with an ionization age and normalization typical for an SNR with an age between 1000 and 8000 yr and a density of $n_{\text{H}} \approx 0.8d_{7.5}^{-3/2} \text{ cm}^{-3}$. Given the X-ray, IR, and radio characteristics of G53.41 + 0.03, we confirm that it is a new Galactic Plane SNR. We do not find a pulsar associated with G53.41 + 0.03, but the upper-limits on the flux density do not exclude the possibility of a young pulsar that is exceptionally weak or not beamed towards Earth.

We also investigate five other SNR candidates from Anderson, et al. (2017) in the same LOFAR FoV. We show that three of these candidates (G52.37 – 0.70, G53.84 – 0.75 and the shell around PWN G54.1 + 0.3) are unlikely to be SNRs and one, G51.21+0.11, is a good SNR candidate that requires further investigation. This demonstrates that it is important to further investigate SNR candidates using low-frequency observations with telescopes such as WSRT and LOFAR.

We would like to thank Vincent Morello, George Heald, Raymond Oonk, Andre Offringa, Jess Broderick, Pedro Salas, Alex Mechev, and Irene Polderman for useful discussions and assistance with LOFAR imaging and calibration. LND and JWTH acknowledge support from the European Research Council under the European Union’s Seventh Network Framework Programme (FP/2007-2013) / ERC Grant Agreement nr. 337062. JWTH is an NWO Vidi fellow. This paper is based (in

part) on data obtained with the International LOFAR Telescope (ILT) under project code LC4_011. LOFAR (van Haarlem et al. 2013) is the Low Frequency Array designed and constructed by ASTRON. It has observing, data processing, and data storage facilities in several countries, that are owned by various parties (each with their own funding sources), and that are collectively operated by the ILT foundation under a joint scientific policy. The ILT resources have benefited from the following recent major funding sources: CNRS-INSU, Observatoire de Paris and Université d’Orléans, France; BMBF, MIWF-NRW, MPG, Germany; Science Foundation Ireland (SFI), Department of Business, Enterprise and Innovation (DBEI), Ireland; NWO, The Netherlands; The Science and Technology Facilities Council, UK. This paper is also based (in part) on observations obtained with *XMM-Newton*, an ESA science mission with instruments and contributions directly funded by ESA Member States and NASA.

Facilities: LOFAR, VLA, WSRT, *XMM-Newton*, *ROSAT*, *Spitzer*

Software: Numpy (Van Der Walt et al. 2011), Astropy (Astropy Collaboration et al. 2013), APLpy (Robitaille & Bressert 2012), WSClean (Offringa et al. 2014), pyBDSF¹⁰, DS9¹¹, SAS v14.0¹², Spex v3.04 (Kaastra et al. 1996), DPPP

REFERENCES

- Acero, F., Ackermann, M., Ajello, M., et al. 2015, *ApJS*, 218, 23
- Anderson, L. D., Bania, T. M., Balsaer, D. S., et al. 2014, *Astrophysical Journal, Supplement*, 212, 1
- Anderson, L. D., Wang, Y., Bihr, S., et al. 2017, *A&A*, 605, A58.
- Arbutina, B., & Urošević, D. 2005, *MNRAS*, 360, 76
- Astropy Collaboration, Robitaille, T. P., Tollerud, E. J., et al. 2013, *A&A*, 558, A33
- Bocchino, F., Bandiera, R., & Gelfand, J. 2010, *A&A*, 520, A71
- Briggs, D. S. 1995, *Bulletin of the American Astronomical Society*, 27, 112.02
- Brogan, C. L., Gelfand, J. D., Gaensler, B. M., Kassim, N. E., & Lazio, T. J. W. 2006, *ApJL*, 639, L25
- Carey, S. J., Noriega-Crespo, A., Mizuno, D. R., et al. 2009, *Publications of the Astronomical Society of Pacific*, 121, 76
- Cash, W. 1979, *The Astrophysical Journal*, 228, 939
- Caswell, J. L. 1985, *Astrophysical Journal*, 90, 1224
- Day, G. A., Caswell, J. L., & Cooke, D. J. 1972, *Australian Journal of Physics Astrophysical Supplement*, 25, 1
- de Plaa, J., Ebrero, J., Grange, Y., et al. 2016, *SPEX Cookbook*
- Dewey, R. J., Taylor, J. H., Weisberg, J. M., & Stokes, G. H. 1985, *ApJL*, 294, L25
- Filipović, M. D., Payne, J. L., Reid, W., et al. 2005, *MNRAS*, 364, 217
- Gerbrandt, S., Foster, T. J., Kothes, R., Geisbüsch, J., & Tung, A. 2014, *A&A*, 566, A76
- Gottschall, D., Capasso, M., Deil, C., et al. 2016, *ArXiv e-prints*, [arXiv:1612.00261](https://arxiv.org/abs/1612.00261) [[astro-ph.HE](https://arxiv.org/abs/1612.00261)]
- Green, D. A. 2005, *Mem. Soc. Astron. Italiana*, 76, 534
- . 2014, *Bulletin of the Astronomical Society of India*, 42, 47

¹⁰ <http://www.astron.nl/citt/pybdsm/index.html>

¹¹ <http://ds9.si.edu/site/Home.html>

¹² <https://www.cosmos.esa.int/web/xmm-newton>

- . 2017, VizieR Online Data Catalog, 7278
<https://www.mrao.cam.ac.uk/surveys/snrs/>
- Gutermuth, R. A., & Heyer, M. 2015, *The Astronomical Journal*, 149, 64
- Hou, L. G., Han, J. L., & Shi, W. B. 2009, *A&A*, 499, 473
- Intema, H. T., Jagannathan, P., Mooley, K. P., & Frail, D. A. 2017, *Astronomy & Astrophysics*, 598, A78
- Kaastra, J. S., Mewe, R., & Nieuwenhuijzen, H. 1996, *UV and X-ray Spectroscopy of Astrophysical and Laboratory Plasmas*, 411
- Kim, H.-J., Koo, B.-C., & Moon, D.-S. 2013, *The Astrophysical Journal*, 774, 5
- Kothes, R., & Foster, T. 2012, *ApJL*, 746, L4
- Kothes, R., Reich, P., Foster, T. J., & Reich, W. 2017, *A&A*, 597, A116
- Lang, C. C., Wang, Q. D., Lu, F., & Clubb, K. I. 2010, *The Astrophysical Journal*, 709, 1125
- Li, Z., Wheeler, J. C., Bash, F. N., & Jefferys, W. H. 1991, *The Astrophysical Journal*, 378, 93
- Lodders, K., Palme, H., & Gail, H. P. 2009, [arXiv:0901.1149](https://arxiv.org/abs/0901.1149)
- Lu, F. J., Wang, Q. D., Aschenbach, B., Durouchoux, P., & Song, L. M. 2002, *ApJL*, 568, L49
- Manchester, R. N., Hobbs, G. B., Teoh, A., & Hobbs, M. 2005, *AJ*, 129, 1993
- Matthews, B. C., Wallace, B. J., & Taylor, A. R. 1998, *The Astrophysical Journal*, 493, 312
- Offringa, A. R., McKinley, B., Hurley-Walker, et al. 2014, *Monthly Notices of the Royal Astronomical Society*, 444, 606
- Onić, D. 2013, *Astrophysics and Space Science*, 346, 3
- Pavlovic, M. Z., Dobardzic, A., Vukotic, B., & Urosevic, D. 2014, *Serbian Astronomical Journal*, 189, 25
- Reed, J. E., Hester, J. J., Fabian, A. C., & Winkler, P. F. 1995, *ApJ*, 440, 706
- Robitaille, T., & Bressert, E. 2012, *APLpy: Astronomical Plotting Library in Python*, *Astrophysics Source Code Library*, [ascl:1208.017](https://ascl.net/1208.017)
- Roman-Duval, J., Jackson, J. M., Heyer, M., et al. 2009, *ApJ*, 699, 1153
- Stil, J. M., Taylor, A. R., Dickey, J. M., et al. 2006, *The Astronomical Journal*, 132, 1158
- Strom, R. G. 1994, *Monthly Notices of the Royal Astronomical Society*, 268, L5
- Strom, R. G. 1994, *A&A*, 288, L1
- Tammann, G. A., Loeffler, W., & Schroeder, A. 1994, *ApJS*, 92, 487
- Taylor, A. R., Goss, W. M., Coleman, P. H., van Leeuwen, J., & Wallace, B. J. 1996, *The Astrophysical Journal*, 107, 239
- Turner, M. J. L., Abbey, A., Arnaud, M., et al. 2001, *Astronomy & Astrophysics*, 365, L27
- Van Der Walt, S., Colbert, S. C., & Varoquaux, G. 2011, *ArXiv e-prints*, [arXiv:1102.1523 \[cs.MS\]](https://arxiv.org/abs/1102.1523)
- van Haarlem, M. P., Wise, M. W., Gunst, A. W., et al. 2013, *A&A*, 556, A2
- van Weeren, R. J., Williams, W. L., Hardcastle, M. J., et al. 2016, *The Astrophysical Journal Supplement Series*, 223, 2
- Vink, J. 2012, *The Astronomy and Astrophysics Review*, 20, 49